

Integrated multi-port multi-wavelength coherent optical source for beyond Tb/s optical links

Received: 11 July 2024

Accepted: 8 June 2025

Published online: 10 July 2025

 Check for updatesAli Pirmoradi¹, Jizhao Zang^{2,3}, Kaisarbek Omirzakhov¹, Zhehao Yu¹, Yan Jin^{2,3}, Scott B. Papp^{2,3} & Firooz Aflatouni¹✉

Microcomb-based sources formed by placing an integrated demultiplexer with an ultra-low power consumption after an efficient optical frequency comb play a key role in many large-scale optical links for data centers and AI systems. Here, we demonstrate a multi-wavelength multi-port source based on a Kerr microcomb followed by a monolithically-integrated demultiplexer, which autonomously locks to and tracks the comb lines. Mach-Zehnder interferometer- and ring resonator-based wavelength demultiplexers, implemented using capacitive optical phase shifters with a zero static power consumption, and a soliton microcomb, with a 200 GHz mode-spacing and 53% efficiency, are implemented. Using a single control unit for the sequential control of all phase shifters, a total demultiplexer power consumption of 2.4 mW is achieved, which corresponds to a record demultiplexer energy consumption of 10 fJ/b and 2.5 fJ/b for an 8-channel and 32-channel systems at a data-rate of 32 Gb/s/channel, respectively, significantly improving the demultiplexer energy efficiency compared to the thermally-tuned state-of-the-art systems.

Wavelength Division Multiplexing (WDM) is a widely adopted technique in optical communication systems for simultaneously transmitting data by use of multiple wavelength channels over a single optical fiber. An essential component of a WDM system is the multi-carrier light source. The spectral purity, number of carriers, wavelength stability, uniformity, and energy efficiency of the multi-carrier light source directly affect the key performance metrics of the link such as aggregate data-rate, bit-error-rate (BER), range, and energy efficiency.

Kerr microresonator frequency combs that generate solitons have been utilized in optical transceivers^{1–10}, and they offer several advantages, ranging from increased data capacity in a small footprint to enhanced signal stability^{11,12}. By laser pumping a high-quality-factor microresonator made of a nonlinear medium, the Kerr effect can be utilized to generate an optical frequency comb, where a series of equally spaced optical carriers, or comb lines/modes, within a single optical channel is formed¹³. The equally spaced coherent comb lines

have a narrow linewidth, making them a good candidate to serve as optical carriers in optical transceivers to significantly increase the aggregate data-rate by introducing many parallel communication channels in a WDM scheme¹⁴. Furthermore, due to the small footprint of Kerr microresonators, transceivers utilizing such devices can achieve a high areal bandwidth density. The high spectral efficiency offered by Kerr microresonators is particularly beneficial in scenarios where there is a growing demand for high-bandwidth applications, such as AI systems, cloud computing, video streaming, and 5G-XG networks^{15–19}. Additionally, Kerr soliton microcombs are typically resilient to external perturbations and can enhance the overall stability of the transmitted signals²⁰, which leads to improved system performance and higher transmission reliability.

In a WDM transmitter, carriers generated within the multi-carrier source are typically separated, individually modulated, and combined to form the transmitter output. Figure 1a shows a simplified block

¹Department of Electrical and Systems Engineering, University of Pennsylvania, Philadelphia, PA, USA. ²Time and Frequency Division, National Institute of Standards and Technology (NIST), Boulder, CO, USA. ³Department of Physics, University of Colorado, Boulder, CO, USA. ✉e-mail: firooz@seas.upenn.edu

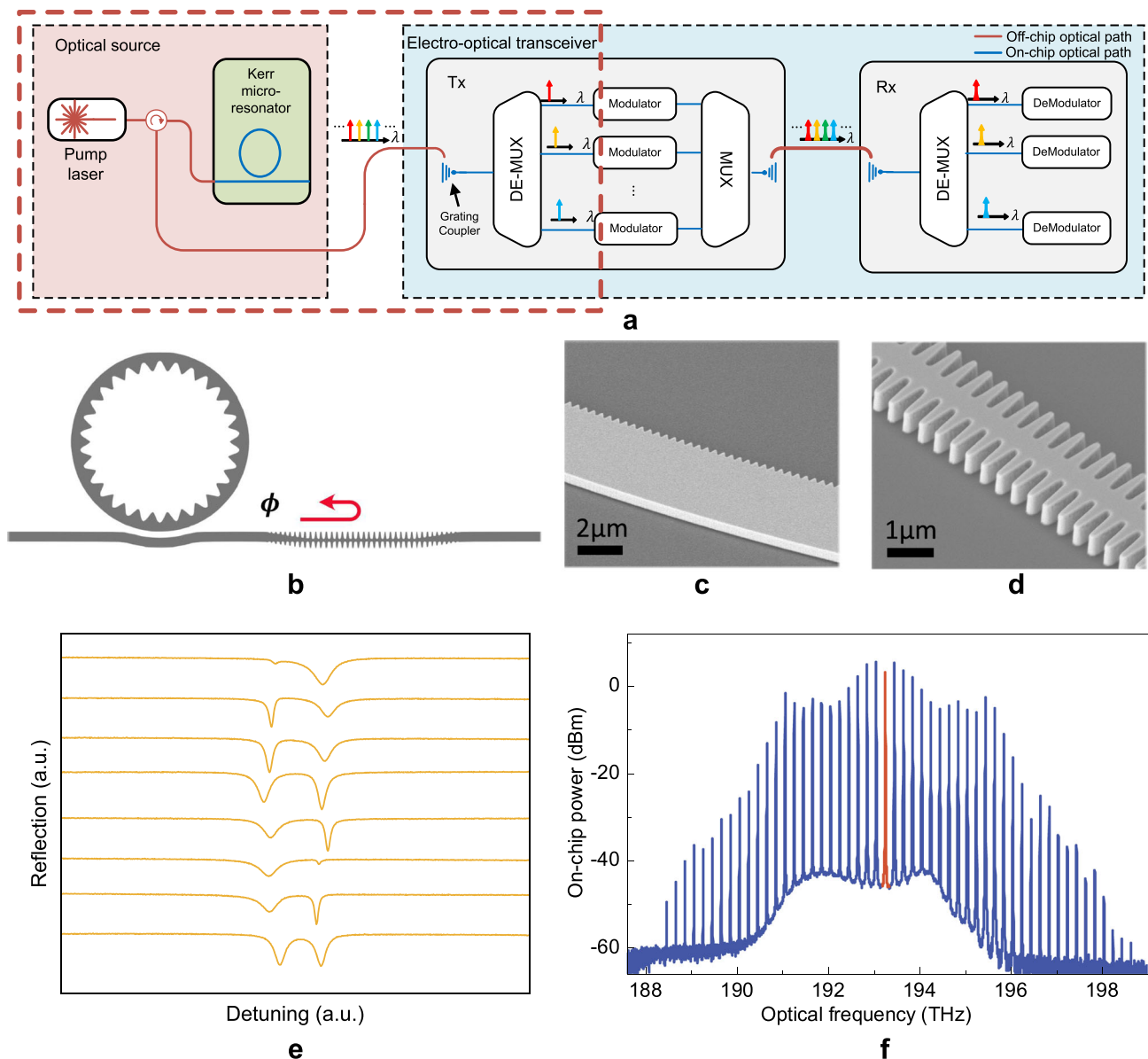


Fig. 1 | Wavelength division multiplexing in a comb-driven transceiver. a The architecture of a Kerr comb-driven WDM transceiver. **b** Schematic of the high-efficiency microcomb generator. **c, d** Scanning electron microscope images of the oscillation on the ring and the bus waveguide reflector, respectively. **e** Measured

reflection spectra when we tune the phase delay ϕ with a step of 0.25π . **f** Optical spectrum of the generated soliton microcomb with a conversion efficiency of about 53%. The residual pump is indicated by the red trace.

diagram of a WDM transceiver that utilizes a Kerr microcomb as the multi-carrier light source, where a demultiplexer (DeMux) placed after the Kerr frequency comb separates the carriers, effectively forming a multi-port multi-wavelength light source. Given the per-carrier data-rate and comb line spacing, the DeMux needs to be designed to provide adequate isolation between different channels to avoid channel-to-channel crosstalk and data corruption. Once the separated carriers are individually modulated, they are combined back together into a single waveguide using a multiplexer (Mux) block. At the receiving end, a similar DeMux block is utilized to separate the modulated carriers before they are delivered to the demodulators for data retrieval.

In the state-of-the-art integrated multiplexing systems, the fabrication process variations as well as temperature fluctuations introduce undesired resonance shift and/or variations in the phase and amplitude of the optical wave²¹, leading to excess insertion loss and crosstalk in the WDM transceivers.

While athermal techniques can be utilized to reduce the need for thermal tuning²², they typically do not compensate for device mismatches caused by process variations, which could be from 5% to 15% for a single-mode waveguide dimension^{23,24}. These mismatches can significantly affect fabrication yield and increase manufacturing costs, particularly in optical links where multiple components (e.g., WDM source, DeMux and Mux in the transmitter, and DeMux in the receiver) need to be precisely wavelength-aligned. Moreover, athermal approaches often come at the cost of increased system size and packaging complexity.

To reduce the undesired effect of process and temperature variations and align the response of the Mux and DeMux with the frequency grid of the multi-carrier light source, often a phase adjustment mechanism is needed. Multiplexer and demultiplexer systems based on thermally tuned Mach-Zehnder interferometers (MZIs) and ring resonators have been demonstrated^{25–30}, that despite excellent

performance and offering a wide tuning range, suffer from a relatively large energy consumption, especially when scaled up to many channels. Furthermore, such systems offer a limited tuning speed (due to the relatively long thermal time constant) and suffer from thermal crosstalk. These undesired effects increase the transceiver complexity and limit the system scalability³¹. Many such systems are implemented through hybrid integration of silicon photonics and CMOS chips via 3D stacking, often using copper pillars, bumps, or by flip chip bonding. Despite excellent performance, certain challenges for hybrid-integrated DeMux and Mux systems, such as packaging parasitics and complexity, and excess power consumption often introduced by the thermal wavelength alignment of devices, remain.

Here, we report the demonstration of two distinct multi-wavelength, multi-port WDM sources, each formed by coupling the output of an efficient Kerr microcomb device to a monolithically integrated demultiplexer, which autonomously locks to and tracks the comb lines using capacitive optical phase tuning with a zero static power consumption. This work advances large-scale WDM transmitter and receiver systems on a fully monolithic platform, offering certain advantages over hybrid-integrated approaches, such as reduced packaging parasitics and complexity, cost, efficiency, yield, and scalability, all while leveraging reliable CMOS platforms without post-processing.

In one design, the Kerr comb device is followed by a Mach-Zehnder interferometer-based wavelength demultiplexer, and in the second design, a ring resonator-based demultiplexer is placed after the Kerr comb output. In both systems, monolithic integration of electronic and photonic devices within the DeMux enables the utilization of capacitive optical phase shifters with zero static power consumption. Both demultiplexers were successfully coupled with the fabricated Kerr comb chip with 200 GHz mode-spacing and 53% efficiency. By utilizing capacitive tuning with zero static power consumption, a single control unit with a power consumption of 2.4 mW for all phase shifters in a sequential control scheme and an efficient locking and tracking wavelength algorithm, the demonstrated monolithic demultiplexers can potentially achieve a record energy consumption of 20 fJ/b for an 8-channel system at 16 Gb/s per channel, which is reduced to 10 fJ/b for a 8-channel system at 32 Gb/s per channel. If the system is scaled to 32 channels with an aggregate data-rate of 1 Tb/s, the energy consumption is further reduced to 2.5 fJ/bit. The implemented scalable system consumes a fixed amount of energy for the entire system, achieving an increased energy efficiency by more than an order-of-magnitude over existing thermally controlled Mux/DeMux systems, which is further improved as the system is scaled to higher data rates.

Results

Kerr frequency microcomb

Recently, Kerr microresonators have emerged as an appealing platform for low-power and chip-scale frequency-comb sources. Benefiting from high quality factor and small mode volume, the threshold power of nonlinear parametric oscillation can be in the milliwatt range³². The nonlinear dynamics of microresonators is described by the Lugiato-Lefever equation (LLE), which predicts several optical states of the microcomb, such as Turing patterns, modulation instability combs, and solitons³³. In particular, soliton microcombs are the most beneficial and resilient for many applications due to their highly coherent comb lines with a high signal-to-noise ratio. Kerr microcombs configured to generate solitons in the normal dispersion regime offer a high degree of spectral flatness at a high conversion efficiency (compared to the microcombs driven in the anomalous regime)³⁴, and as such are a good candidate to serve as a multi-carrier light source in a WDM system. In this work, to enable phase matching for soliton formation in a normal-dispersion microresonator, we implemented a photonic-crystal resonator (PhCR). As shown on Fig. 1b, the PhCR is formed by adding a uniform grating pattern on the inner

wall^{13,35}. The grating pattern forms a one-dimensional photonic crystal, which introduces coupling between the clockwise and counter-clockwise propagating modes of light, leading to a mode splitting at azimuthal mode of $\lambda_{\text{PhC}} = 2n_{\text{eff}}\Lambda$, where n_{eff} is the effective refractive index and Λ is the grating period. Pumping the red-shifted (lower-frequency) mode meets the phase-matching condition and results in spontaneous soliton formation in PhCRs³⁵.

The benefit of high conversion efficiency is the improved per-comb-line power for a given pump power. We define the pump-to-comb conversion efficiency as $\eta = P_{\text{comb}}/P_{\text{pump}}$, where P_{comb} is the comb power and P_{pump} is the on-chip pump power. For a flat comb, the per-comb line power can be estimated as $\eta P_{\text{pump}}/N_{\text{lines}}$, where N_{lines} is the number of comb lines. Depending on the specific applications, we can control N_{lines} by engineering the microresonator dispersion. In chip-scale WDM transceivers, the available pump power is usually limited to tens of milliwatts. Given a fixed P_{pump} and N_{lines} , a higher conversion efficiency allows for higher per-comb-line power, which is beneficial to the SNR on the receiver side and allows for longer transmission distance and lower BER. Although the PhCR device is capable of low-noise flat frequency comb generation, it has a limited conversion efficiency since (as confirmed by simulation) most of the pump power exits the ring and propagates in the forward direction at the soliton state. We have previously shown a PhCR with a bus waveguide reflector to increase the conversion efficiency^{36,37}, and we use a similar scheme for the demonstrations here (Fig. 1b).

The high-efficiency soliton generator (including the photonic crystal resonator followed by the reflector) is fabricated on an air-clad tantalum pentoxide (Ta_2O_5 , hereafter tantala) material platform³⁸. Tantala is CMOS-compatible material that has a wide transparent window from 300 nm to 8000 nm. Compared with other photonic materials such as silicon nitride, it offers several superior material properties, such as a three times higher nonlinear index, lower stress, and smaller thermo-optic coefficient. The width of the micro-ring resonator is 4 μm and the ring radius is 109.5 μm , corresponding to a free spectral range of 200 GHz. Figure 1c and d show scanning electron microscope (SEM) images of the grating structure on the inner wall and the bus waveguide reflector, respectively. The grating depth on the inner wall of the micro-ring resonator is 275 nm, leading to a mode splitting of 900 MHz. Despite the internal loss introduced by the grating pattern, our devices can still achieve an intrinsic quality factor of 2.6 million. The waveguide reflector has a 3-dB bandwidth of 5 THz, peak reflectivity of is 90%, and a central frequency that is aligned with the pump mode at 193.3 THz. The optical phase delay (ϕ) of the reflector plays an important role in determining η . We design eight devices so that the phase delay varies from 0 to 2π with a step size of 0.25π . Both simulation and experiment indicate that our devices can maintain a high conversion efficiency over a broad range of phase delay ($\sim 0.75\pi$). Despite the fabrication uncertainties, at least one device among eight can achieve high conversion efficiency. We sweep ϕ (by adjusting the ring-reflector distance or rotating the PhCR) and measure the reflection with an oscilloscope. Figure 1e shows a superposition of the oscilloscope traces in the cases with different ϕ , confirming that we can selectively modify the coupling of the two split modes. To minimize the interference of the blue (higher-frequency) mode and maximize the achievable comb efficiency, we choose ϕ that under-couples the blue-shifted mode but over-couples the red-shifted mode.

Since the soliton preferably propagates in the backward direction, we use a circulator before the input lensed fiber to extract the backward-propagating comb³⁶. Figure 1f presents the spectrum of a backward soliton microcomb that achieves 53% conversion efficiency. Note that our design eliminated the need for a pump rejection filter as the residual pump (red trace in Fig. 1f) is lower than other comb lines. The on-chip pump power is 48 mW, which is compatible with the high-power distributed-feedback (DFB) lasers for hybrid integration. In the

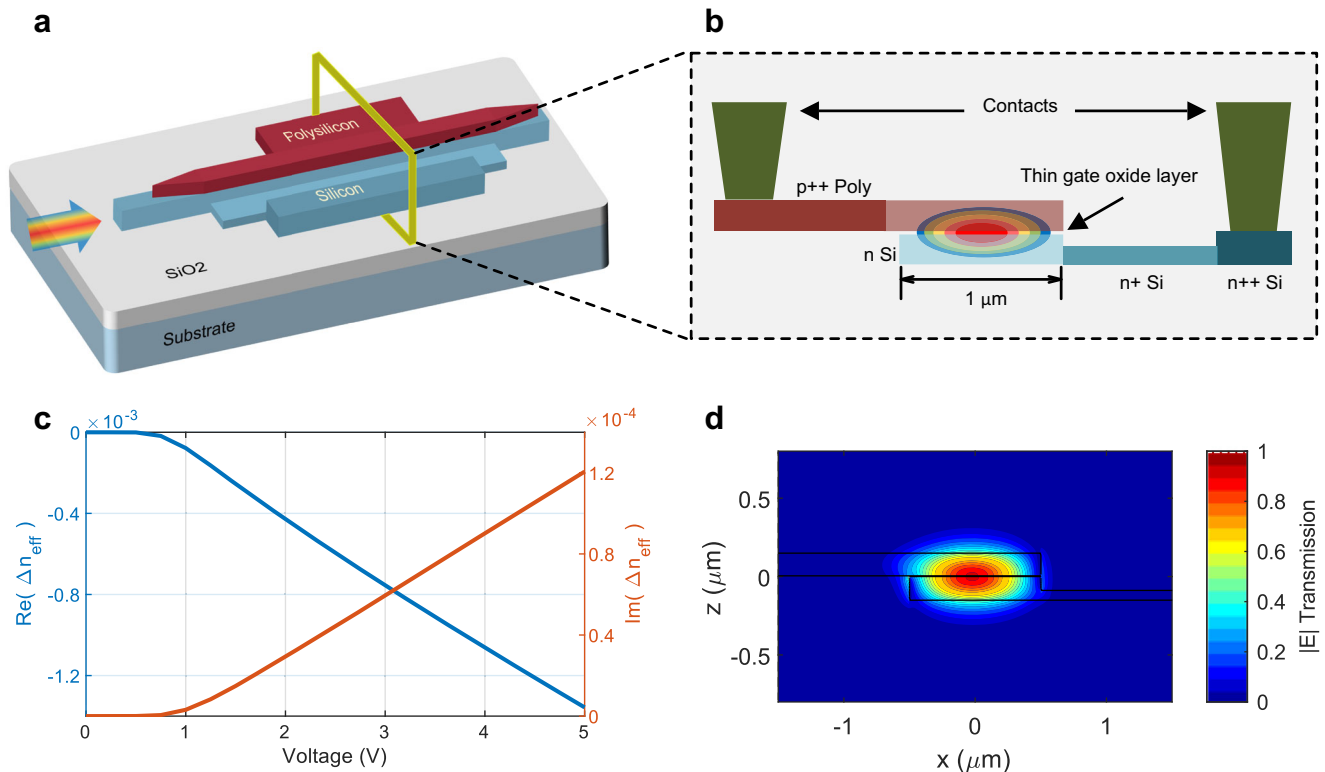


Fig. 2 | Capacitive optical phase shifter. **a** Structure of the implemented capacitive optical phase shifter. **b** Cross-section of the capacitive phase shifter. **c** Simulated effective real and imaginary parts of the refractive index as a function

of the applied bias. **d** the profile of the magnitude of the electric field of the TE mode in the capacitive phase shifter.

experiment, we use an erbium-doped fiber amplifier (EDFA) due to the fiber-to-chip coupling loss (4.5 dB/facet) and the low output power (10 mW) from our laser diode. We can avoid using an EDFA by employing a laser with higher output power, designing oxide-clad device to reduce the coupling loss to below 2 dB/facet, and increasing the quality factor of our PhCR for a lower threshold power. In our experiment, we connect the comb chip to the DeMux system chip via optical fiber. We are in the process of developing robust silicon oxide claddings for the tantalum comb chip, which would enable a variety of packaging and integration options. In particular, our platform already enables sophisticated nanophotonic designs; hence grating couplers between the comb chip and DeMux chip can be designed and optimized for integration.

Mux/DeMux systems

In this work, we design and implement two different Mux/DeMux architectures, both monolithically integrated on GlobalFoundries 90 nm CMOS-SOI process. Each architecture incorporates capacitive optical phase shifters with zero static power consumption to address optical length errors caused by fabrication process variations and temperature drift. Conventional multiplexing systems utilizing cascaded ring resonators controlled by heaters^{39,40} achieve low insertion loss and channel-to-channel crosstalk but exhibit high energy consumption due to the utilization of thermal phase shifters. Furthermore, managing thermal crosstalk between channels proves to be a significant practical challenge. To overcome these challenges, as the first design, a DeMux/Mux system with cascaded ring resonators is devised that incorporates capacitive optical phase shifters formed using semiconductor-insulator-semiconductor capacitor (SISCAP) structures. Despite offering zero static power consumption, given the FSR of the micro-rings, the tuning range of the SISCAP-based micro-ring resonators is limited by various parameters such as bend radius, doping levels, and the micro-ring circumference. The second design is

based on asymmetric Mach-Zehnder interferometers (MZI) with SISCAP phase shifters, where a higher tuning range compared to the first design is achieved at the cost of a larger chip area and a more complex wavelength locking process.

The design and performance evaluation of each system includes measurements of total power consumption, optical insertion loss, and channel-to-channel crosstalk when placed after the integrated Kerr microcomb, which are discussed next.

Capacitive phase shifter

A key component of our designs, enabling zero static power consumption, is the capacitive phase shifter. While vertically fabricated capacitive phase shifters have been previously demonstrated^{41,42}, the monolithic integration of the system on a CMOS process allows for the utilization of the thin gate oxide layer that enables implementation of SISCAP phase shifter next to the control electronics.

The architecture of the implemented SISCAP phase shifter is shown in Fig. 2a, where a tapered gate polysilicon waveguide, placed on top of the silicon waveguide, is used to transition the wave from a single-mode silicon rib waveguide to a polysilicon-on-silicon ridge waveguide. The cross-section of this device is shown in Fig. 2b, where the optical mode is partially formed within the silicon and polysilicon regions. In this configuration, the thin gate oxide layer separating the polysilicon from silicon serves as the insulator in the silicon-oxide-polysilicon capacitor without interfering with the optical mode. Consequently, by applying a DC voltage across the formed capacitor, the charge distribution overlapping with the optical mode can be adjusted, which alters the effective index of refraction of the medium and introduces an optical phase shift. The thin gate oxide layer blocks the DC current and results in optical phase tuning with zero static power consumption. Figure 2c illustrates the simulated real and imaginary parts of the effective refractive index as a function of the applied voltage across the capacitive phase shifter for the case that waveguide

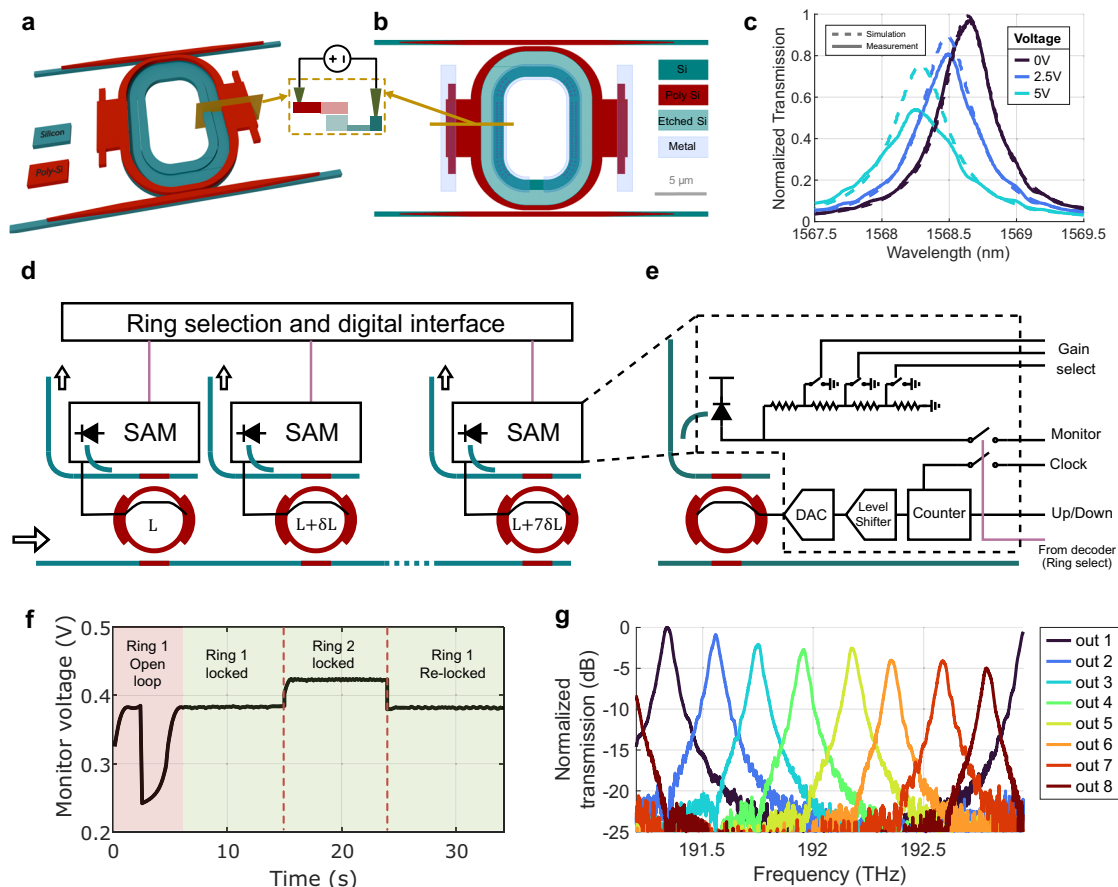


Fig. 3 | Capacitively tuned micro-ring resonator based DeMux. **a** 3D schematic of the adiabatic drop micro-ring resonator with capacitive phase shifter. **b** The layout of the micro-ring resonator. **c** Simulated and measured capacitive ring tuning response. **d** Block diagram of the implemented 8-channel DeMux based on capacitively tuned adiabatic ring resonators. Two consecutive ring resonators are slightly different in circumference by length of δL such that their corresponding

resonance frequencies are on the comb frequency grid. **e** Block diagram of the sensing, actuation, and memory (SAM) unit used for control and tuning of the micro-rings. **f** Sequential locking demonstration for the ring based DeMux. **g** The outputs spectra of the 8-channel ring-based DeMux after sequential wavelength alignment.

width is set to $1\ \mu\text{m}$, showing the tradeoff between the amount of optical phase shift and propagation loss introduced by the capacitive phase shifter. Figure 2d shows the optical mode formed within the silicon-oxide-polysilicon waveguide. Note that this design can be implemented in devices with both straight and bent waveguides, such as Mach-Zehnder Interferometers (MZIs) and ring resonators, respectively.

Cascaded micro-ring Mux/DeMux

The first implemented Mux/DeMux architecture is based on eight cascaded capacitively tuned adiabatic micro-ring resonators with minor circumference variations^{43,44}. A three-dimensional schematic of the implemented capacitively tuned adiabatic ring resonator is illustrated in Fig. 3a, where a SISCAP is integrated within the ring section. The adiabatic structure of the ring enhances the quality factor, thereby improving the isolation between channels in the Mux/DeMux configuration. The top-view layout of the implemented micro-ring resonator is shown in Fig. 3b. The device consists of two similar couplers with a coupling length of $2\ \mu\text{m}$, coupling gap of $0.14\ \mu\text{m}$, bend radius of $5\ \mu\text{m}$, and a straight section of about $5.7\ \mu\text{m}$.

In Fig. 3c, the tuning response of the capacitively tuned ring resonator is shown, where a quality factor of approximately 3.6k at 0V and an average tuning slope of $130\text{pm}/\text{V}$ for a ring with an FSR of 12.8nm is achieved. A maximum tuning range of 650pm (at 5V) is achieved, which is limited by the capacitor breakdown voltage. This tuning range proved to be sufficient for compensating temperature

drifts in our measurements. Furthermore, by careful selection of ring dimensions, the resonances of the micro-rings were aligned with the comb lines eliminating the need for local heaters, which results in a significant reduction in power consumption.

Figure 3d shows the implemented 1:8 DeMux constructed using eight capacitively tuned adiabatic rings cascaded on the input bus waveguide, allowing for the separation of the eight carriers at the drop ports of the rings. A control unit sequentially selects and capacitively tunes and locks the rings to the corresponding carrier wavelength, which significantly reduces the chip area and power consumption.

A sensing, actuation, and memory (SAM) unit is placed next to each micro-ring. The block diagram of the SAM unit is shown in Fig. 3e. During the sequential control of the rings, one SAM unit is selected at a time by a global decoder which is placed in the selection and digital interface block. Once a SAM unit is selected, a photodiode (monitoring 5% of the drop port output of the ring) is employed to monitor the status of the ring. The photocurrent is converted to a voltage (i.e., monitor voltage) using a shunt resistor. Depending on the error signal, defined as the difference between the monitor voltage and the desired preprogrammed reference voltage, an up/down signal is generated which is routed to a 5-bit up/down counter. The counter output is adjusted using a 5-bit digital level shifter and then converted to an analog voltage (between 0 to 5V) using a resistive-ladder digital-to-analog converter (DAC). The DAC output drives the capacitive phase shifter. Once the ring is locked to the desired wavelength, the data is latched into the counter, serving as a local memory, which

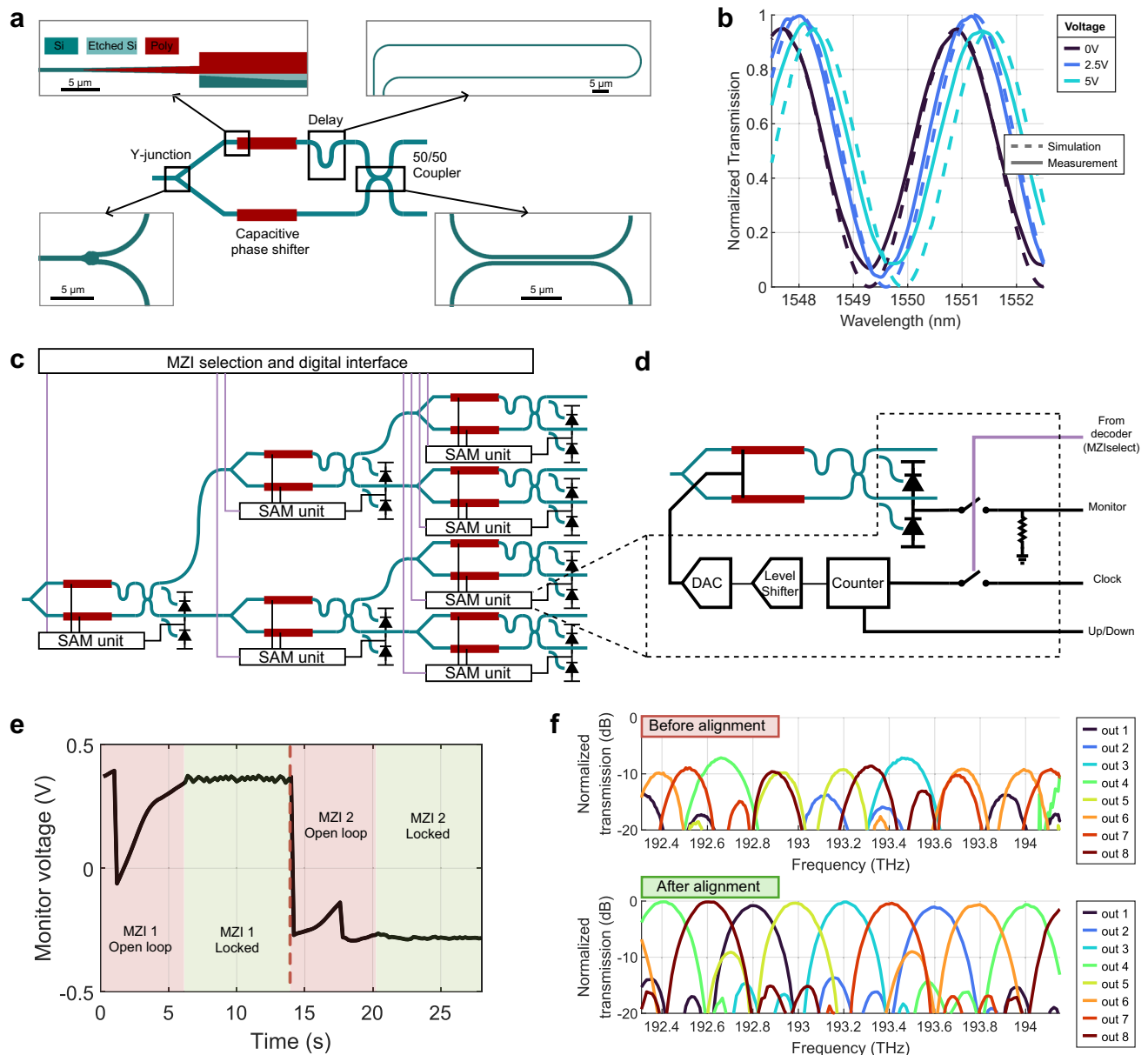


Fig. 4 | Capacitively tuned MZI based DeMux. **a** Schematic of the capacitively controlled MZI and layout of Y-junction, phase shifters, delay line, and coupler. **b** Simulated and measured capacitive MZI tuning response. **c** Block diagram of the implemented 8-channel DeMux based on capacitively tuned MZIs. **d** Block diagram

of the MZI control unit (SAM). **e** Sequential locking demonstration for the MZI-based DeMux with single-tone tunable laser as the input of the system. **f** The outputs spectra of the 8-channel MZI-based DeMux before and after wavelength tuning.

maintains the ring at the set point. Subsequently, the central decoder selects the next ring within the sequence for wavelength locking, and the process is sequentially repeated.

The first time the SAM unit of each ring is selected, the voltage across the capacitive section is chirped to find the maximum monitor voltage (corresponding to the peak of the ring response). This maximum monitor voltage is recorded and stored, and the feedback loop is engaged to keep the monitor voltage locked to the recorded value. Figure 3f shows the measured sequential locking process for two rings. In this case, after both rings are sequentially locked, the central control unit selects the first ring to check its status and dynamically adjusts the bias point if necessary. It is important to note that when a ring is deselected, it is disconnected from the off-chip clock, as a result, the dynamic power consumption of the corresponding SAM unit drops to zero. Therefore, at any given time, only one SAM unit is active, significantly reducing the overall power consumption of the system. Note

that in this measurement the data acquisition is slowed down to ease the illustration. Note that this wavelength locking mechanism is also applicable to a cascaded ring-based Mux system. The only difference is that for the Mux system, the monitor voltage is acquired from a sniffer photodiode on the bus waveguide following each ring. Figure 3g shows the outputs spectra of the 8-channel ring-based DeMux after sequential wavelength alignment.

Mach-Zehnder tree DeMux/Mux

The block diagram of the second Mux/DeMux architecture is shown in Fig. 4a, which is implemented based on binary tree formation of capacitively tuned unbalanced MZIs⁴³. Each MZI consists of a Y-junction at the input, which evenly splits the incoming light into two single-mode waveguide arms, with an excess loss of about 0.3 dB⁴⁵. Subsequently, both arms are tapered into 100 μm long SISCAP phase shifters, formed using a multimode waveguide with a width of 1 μm .

The light is tapered back to single-mode waveguides (with a width of 0.5 μm) after the phase shifters. To create a periodic wavelength response that matches the target FSR (set by the comb mode spacing), a delay line is incorporated in the top arm. Finally, the outputs of the two arms are combined using a 50/50 directional coupler. The simulated and measured response of the capacitive MZI for different voltages applied to the SISCAP is shown in Fig. 4b, where a tuning efficiency of about 160 pm/V for an MZI with an FSR of 3.2 nm is achieved. In other words, the capacitively tuned MZI can be tuned by about 0.25FSR when the voltage across the capacitive section is set to 5 V, which in our experiments was sufficient to compensate for the process variations and typical temperature fluctuations.

Figure 4c depicts the block diagram of the 8-channel DeMux/Mux system implemented by cascading three stages of capacitively tuned unbalanced MZIs in a binary tree formation. By tuning the response of the MZIs to their corresponding wavelength grid, the even and odd comb lines are separated at the outputs of each MZI. The delay difference between the arms of each MZI stage is designed to ensure effective separation of the 8 input optical carriers while minimizing the insertion loss and crosstalk.

The length difference between the arms of the MZI (setting the delay imbalance) in the first layer, L_1 , is set such that its FSR is twice the comb mode spacing, which results in the separation of even and odd lines on the two outputs of the first MZI once the MZI is accurately tuned and aligned with the input comb lines. This process is repeated for the second and third layers of the MZIs. The length difference between the arms of the MZIs in the layer i is written as $L_i = L_1/2^{i-1}$. Note that the MZIs within the layer i are designed to exhibit almost the same FSRs. The slight FSR difference, realized by creating a small difference in delay lengths (δL_i), is introduced to passively set the phase difference between the arms of the MZI close to the desired operating point, thereby reducing the requirements for the tuning/locking range.

Similar to the ring-based system, each MZI is accompanied by a SAM unit. A central on-chip decoder sequentially selects the SAM units to be engaged in a feedback loop. The goal is to dynamically set the drive voltage of the capacitive phase shifter of the corresponding MZI such that the output power remains at the desired pre-stored reference value. In the SAM subsystem shown in Fig. 4d, for each MZI, 5% of the MZI output is sampled and detected using a balanced photodiode (BPD) and the output photocurrent is converted to a voltage (i.e. monitor voltage) using a shunt resistor. Meanwhile, for the unselected MZIs, the BPD output is grounded through a shunt transistor switch. The monitor voltage is then compared with the stored reference voltage using a comparator in the central unit, which sets the UP/DOWN signal of the counter. The output of the 5-bit counter is adjusted by a level shifter to a 0–5 V range and then converted to an analog voltage using an R-2R DAC. The DAC output differentially drives the SISCAP and tunes the MZI.

As shown in Fig. 4e, during the open-loop calibration phase of the wavelength tuning and locking of the MZIs, the SAM unit of MZIs are sequentially selected, the driving voltage of their phase shifter is swept while the voltage across the resistor at the SAM unit output (which is proportional to the balanced photodiode photocurrent) is monitored and the optimum monitored voltage (i.e. the desired operating point) is recorded. Then, in the closed loop phase, the MZI phase shifter is locked to the desired operating point. Note that, unlike the ring resonators, in an MZI with an FSR twice of the comb mode spacing, the highest output power does not necessarily correspond to the optimal alignment. In fact, in an ideal case with a perfectly flat optical comb and a lossless MZI with an FSR that is precisely twice the comb mode spacing, the optical power at each output of the MZI is consistently half of the total power of the comb, irrespective of the phase difference between the MZI arms. This is discussed in more details in the Method section. Figure 4f shows the response of the 1-to-8 MZI-based DeMux before and after the wavelength alignment process.

While elegant techniques like MZI triplets⁴⁶, and ring-assisted MZIs⁷ have been proposed for locking MZI binary tree structures to a multi-wavelength source, they typically suffer from high power consumption, large footprint and implementation challenges. Furthermore, methods such as MZI triplets⁴⁶ typically require a multi-wavelength source with an equal per carrier power for effective wavelength locking, which limits their applications since, in practice, implementation of an optical frequency comb with an equal power distribution across all lines is challenging.

In this work, a tuning and locking mechanism is implemented that aligns the DeMux/Mux system with an optical Kerr frequency comb with a non-uniform power distribution across the lines. The process has two phases of peak search (using the pump laser) and comb acquisition and tracking (where the system is locked to the comb lines).

During the peak search phase (Fig. 5a), first the comb is deactivated, in which case, the optical input to the MZI-tree DeMux is only the tunable single tone pump laser. Then, MZIs within the DeMux system are selected one at a time in the order of input layer to the output layer. For each selected MZI, the pump wavelength is set to the corresponding target wavelength (matching the wavelength of one of the comb lines), and the voltage across the capacitive phase shifter of the selected MZI is ramped up using the on-chip counter (triggered by the off-chip micro-controller) until the MZI optical output power is maximized, for which case the count number for the selected MZI is recorded. The process is repeated for all MZIs and the resulting count numbers aligning MZIs with the corresponding target wavelengths are recorded. Finally, the recorded count numbers from the peak search are loaded into the counter of each MZI within its SAM unit, tuning the peak response of each MZI to its target wavelength.

In the comb acquisition and tracking phase (Fig. 5b), which is performed right after the peak search phase, the comb is activated and the peak in the response of each MZI is tuned to the same wavelength as the end of the peak search phase (based on loaded count values aligning each MZI with its target wavelength in the peak search phase). Then, the monitor voltage corresponding to the output power of each MZI is stored in a memory unit as the MZI locking reference voltage. These reference voltage values are exclusive to each MZI and correspond to the comb power in the state of the best alignment. During the normal operation of the system, MZIs are sequentially selected and, if needed, each MZI is tuned in a feedback loop such that the monitored voltage corresponding to the MZI output power matches its stored reference value.

In our experiments, the output power of each MZI was monitored every 2 min, and under stable conditions, no MZI alignment with the comb lines was needed for at least 90 min. Note that in case of a comb power profile change or a large enough temperature variation, the reference values may need to be updated. In our multiple hour-long experiments, the reference adjustment was only performed at the start of the measurement (as a calibration process).

Multi-wavelength multi-port light source

Two multi-port multi-wavelength light sources are formed by use of the two different DeMux systems placed after the implemented Kerr comb device. Figure 6a shows the block diagram of the measurement setup used for characterization of multi-wavelength multi-port light source implemented by placing cascaded micro-ring resonators after a Kerr frequency comb. The output of a DFB laser emitting at about 1550 nm is amplified and serves as the pump signal for comb generation. After polarization adjustment, the pump is edge-coupled to the tantalum chip, and the generated frequency comb is edge-coupled from the tantalum chip to a single mode fiber, passed through a circulator, polarization adjusted, and coupled from the fiber to the silicon photonic chip through a grating coupler. Note that additional comb modes (besides the target optical carriers) should be filtered before the

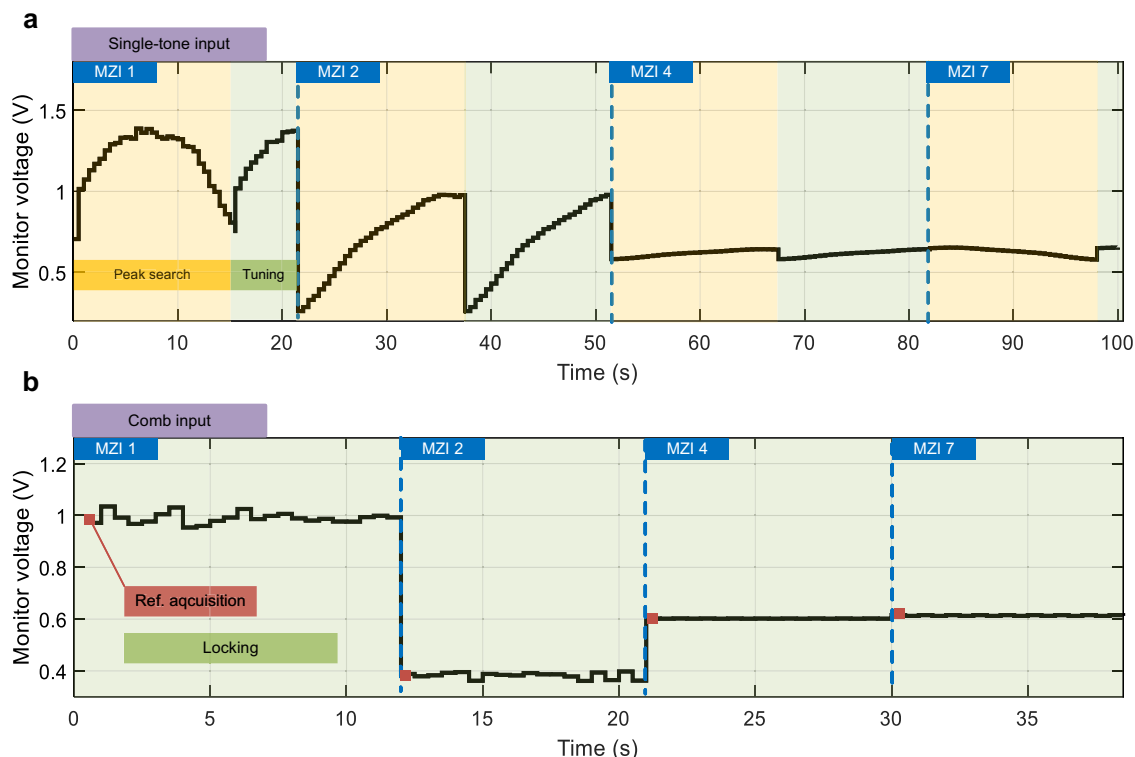


Fig. 5 | Peak search, comb acquisition, and tracking in the MZI-based DeMux.

a In the peak search process (yellow regions), the comb is deactivated and for each MZI, the tunable pump laser is tuned to the wavelength of the corresponding target comb line and the MZI phase shifter voltage is ramped up covering the tuning range and the count number corresponding to the voltage that aligns the peak in the MZI response to the corresponding target wavelength is recorded. During the tuning process (the light green regions), while the comb is inactive, the counter counts to

the recorded count number aligning the MZI with the target wavelength. **b** In comb acquisition phase (red dots), the comb is activated and the monitor voltage corresponding to the output power of each MZI, the locking reference voltage, is stored in a memory unit. During the tracking process (the light green region), MZIs are sequentially selected and, if needed, the monitor voltage of each MZI is locked to the corresponding locking reference voltage using the counter up/down signal in a feedback loop.

DeMux to avoid introducing interference in the transmitter system. The coupled light is routed to the DeMux system using nanophotonic waveguides. Different comb lines are separated at the output of the DeMux and routed to the 8 outputs of the multi-port light source. A portion of the light from each output port is coupled out of the chip using a sniffer coupler, followed by a grating coupler, and is monitored by an optical spectrum analyzer (OSA). The capacitively tuned micro-ring resonators within the DeMux are autonomously aligned with the wavelength of corresponding comb lines using the on-chip SAM units. Figure 6b shows the microphotograph of the ring-resonator-based DeMux chip implemented using GlobalFoundries GF9WG 90 nm CMOS SOI process.

Figure 6c shows the measurement results for the implemented ring-based multi-port multi-wavelength light source, where comb lines are successfully separated and a crosstalk of better than 15 dB is achieved. Depending on the measurement conditions, occasional periodic tuning control is autonomously initiated (e.g., every hour in this case) to ensure that alignment is preserved.

Figure 7a shows the block diagram of the measurement setup used for characterization of the multi-port multi-wavelength light source implemented by placing an MZI binary tree DeMux after the implemented Kerr frequency comb, where the optical frequency comb output (generated the same way as in Fig. 6a is polarization adjusted and coupled into the DeMux chip through the on-chip grating coupler. The separated comb lines are routed to the output waveguides, coupled out using the sniffer directional couplers, followed by grating couplers, and monitored on an OSA. Figure 7b shows the microphotograph of the MZI-based DeMux chip implemented using GlobalFoundries GF9WG 90 nm CMOS SOI process. Figure 7c shows the

measurement results for the implemented MZI-based multi-wavelength multi-port light source, where a crosstalk of better than 11 dB is achieved.

Note that while the frequency selectivity of the subsequent stages (e.g. ring modulators) results in higher overall isolation, the channel-to-channel isolation of the proposed ring and MZI based DeMux systems could be improved by increasing the quality factor of the rings (limited partially due to the loss of the capacitive modulators, which could be improved by adjusting the capacitive modulator structure and doping levels), increasing the bandwidth of the directional couplers (using directional couplers with broadband bends), and/or adjusting the ring coupling ratio (at a cost of higher drop-port insertion loss). Furthermore, utilization of more complex devices such as ring-assisted MZIs could improve the isolation.

Despite having a larger footprint of $0.19 \times 0.03 \text{ mm}^2$ per MZI, incorporating MZIs in a 3-layer DeMux system results in an insertion loss of 4.5 dB (1.5 dB per layer) and crosstalk of better than 11 dB compared to the ring resonator-based DeMux, which has a smaller footprint of $0.02 \times 0.03 \text{ mm}^2$ per ring resonator, and a crosstalk better than 15 dB but introduces a 7 dB insertion loss. In both systems, a zero static power consumption for capacitive tuning of micro-rings or MZIs for the 8-channel Mux or DeMux is achieved while the control electronics has a power consumption of under 2.4 mW (primarily consumed by the on-chip digital circuitry). Note that no thermoelectric cooler (TEC) was used for the multiplexer chips.

Summary and Discussion

We have designed and implemented two multi-wavelength multi-port light sources formed by using a highly efficient Kerr micro comb

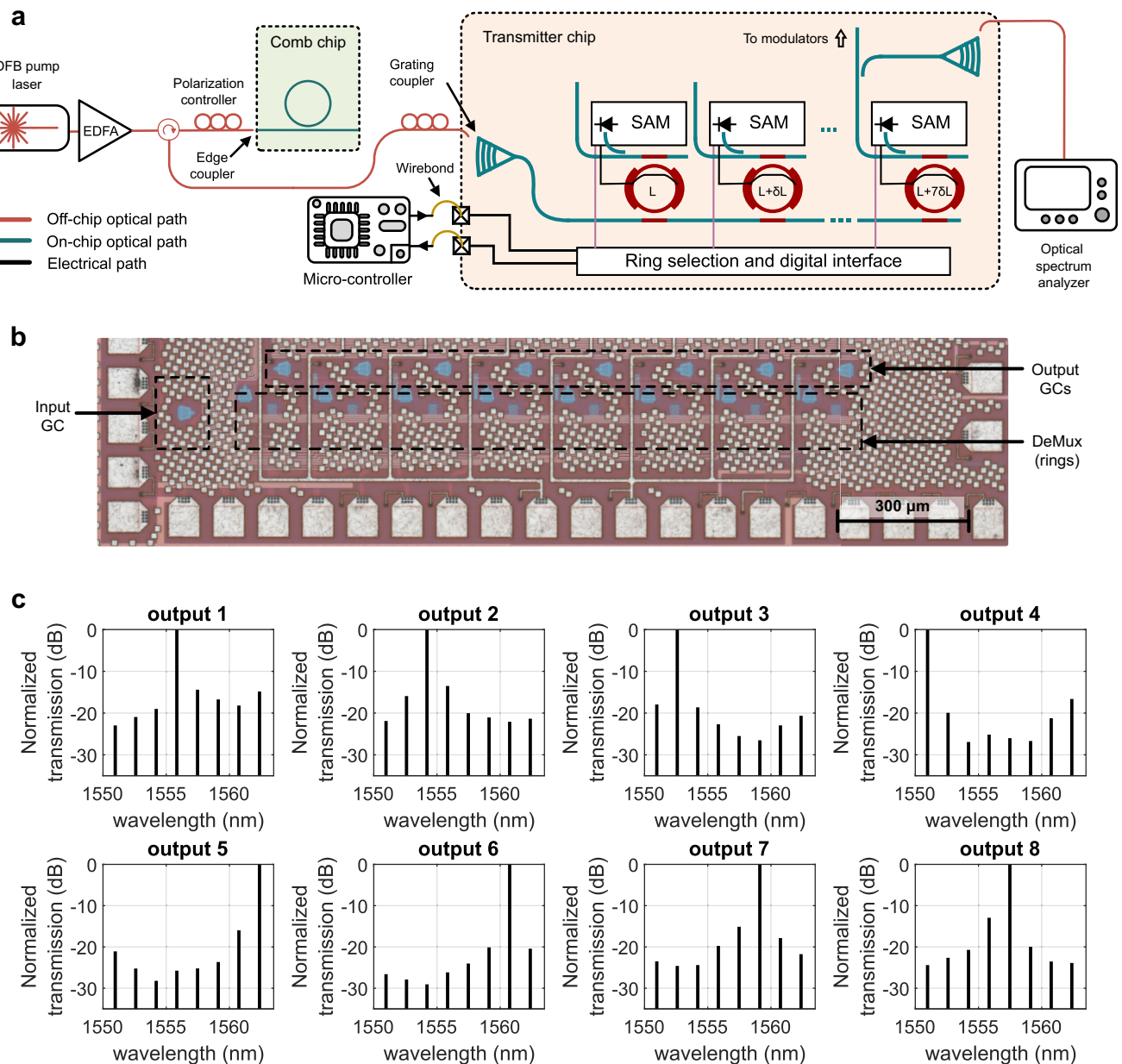


Fig. 6 | Characterization of micro-ring based multi-wavelength multi-port source. a Measurement setup. The optical comb is coupled to the ring-based 1:8 DeMux, and a fraction of each output is coupled off-chip and monitored using an

optical spectrum analyzer. **b** Microphotograph of ring-resonator-based DeMux chip. **c** Normalized spectra of 8 comb lines separated using the ring-based DeMux.

device ($\eta \sim 53\%$) implemented on tantalum with a 200 GHz mode-spacing followed by two different monolithically integrated DeMux systems that utilize a scalable capacitive tuning scheme with zero static power consumption and a small footprint. The two DeMux designs are based on adiabatic micro-ring resonators and a binary tree MZI structures, respectively. While micro-rings offer advantages such as smaller footprint, higher channel-to-channel isolation, and a less complex wavelength locking process, MZIs are more resilient to fabrication process variations and thermal fluctuations.

FDTD simulations show that a longer coupling region in capacitively tuned micro-ring resonators within the Mux/DeMux structure reduces the system overall insertion loss to about 2 dB while maintaining more than 12 dB channel-to-channel isolation. We have included methods for further reducing the crosstalk in Supplementary Note 2.

Furthermore, the SISCAP phase shifters within the micro-ring resonators could be modified to include the bent regions of the micro-ring, resulting in a higher capacitive tuning range.

For the case that implementation of a multi-wavelength source with a larger number of ports is designed, a flat Kerr comb with a larger number of lines followed by a hybrid architecture of MZIs and micro-ring resonator based DeMux/Mux systems can be utilized (e.g. a 1:32 DeMux formed using a 1:4 MZI based DeMux followed by 4 parallel 8 inline micro-ring ring DeMux structures) enabling massively scalable WDM communication links while preserving performance. Note that considering the bandwidth of the ring/MZI (which is about 50 GHz in this work), for a given modulation format, there is a maximum data-rate for which the proposed demultiplexer could also be used as a multiplexer after the modulators in the transmitter for an error-free operation.

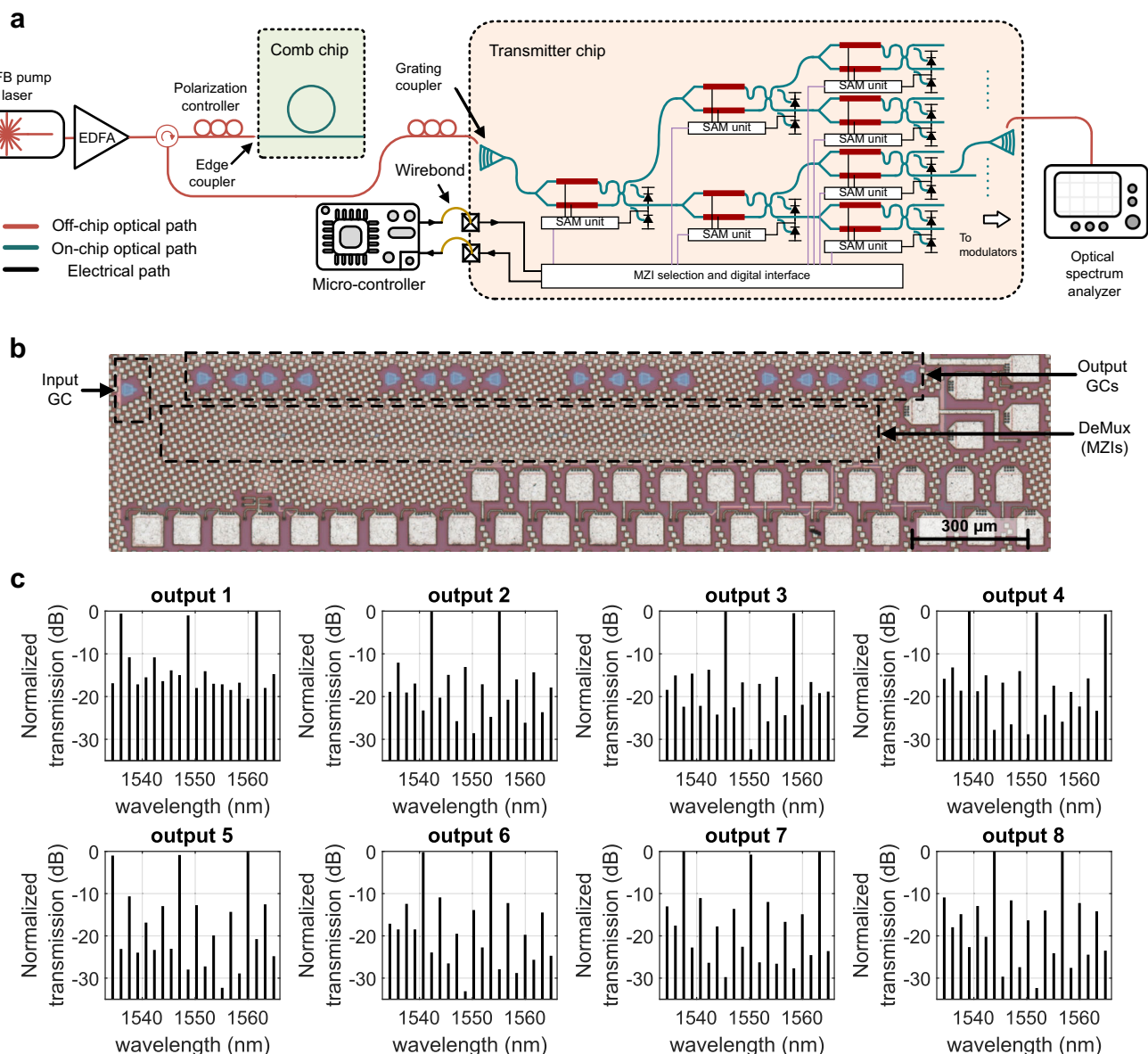


Fig. 7 | Characterization of MZI based multi-wavelength multi-port source. **a** Measurement setup. The optical comb is coupled to the MZI-based 1:8 DeMux, and a fraction of each output is coupled off-chip and captured by an optical

spectrum analyzer. **b** Microphotograph of the MZI-based DeMux chip. **c** Normalized spectra of 8 DeMux outputs, where at each output, one in every 8th comb lines are selected.

Methods

Chip fabrication

The DeMux/Mux systems were monolithically integrated using Global Foundries 9WG CMOS-SOI silicon photonic process. This technology offers devices with an f_T of up to 150 GHz⁴⁷, suitable for both RF modulation and demodulation on the same chip with the DeMux/Mux systems and relevant electronics, enabling implementation of monolithic transceivers with a reduced packaging complexity.

Photonic waveguides with approximately 1.7 dB/cm loss at wavelengths around 1550 nm, grating couplers with a coupling loss of approximately 5 dB, and photodiodes with a responsivity of about 0.9 A/W were utilized.

Our air-clad PhCR devices were fabricated in the tantala material platform. Our fabrication begins with oxidized silicon wafers (3 μm SiO₂ on Si) where the tantala device layer is ion-beam sputtered to the desired 570 nm thickness. The devices are patterned using electron-beam lithography (EBL) and etched using inductively-coupled-plasma (ICP) reactive-ion-etching (RIE) on a 75 mm tantala wafer. The wafer is

chemically (EKC265) and O₂ plasma cleaned, followed by a long annealing step in an oxygen-nitrogen mixture atmosphere to improve the optical loss. Our fabrication process enables wafer-scale fabrication with high device yield and good consistency.

Capacitive phase shifter efficiency

In capacitive phase shifters, to find the change in the effective refractive index as a function of applied voltage, the distribution of free carriers is captured at various bias points using the Lumerical CHARGE toolbox, and the obtained charge distribution results are imported into the Lumerical MODE toolbox. In MODE, the eigenmodes of the waveguide are simulated, and the electro-optical effect is calculated using the Plasma-Drude model for silicon⁴⁸.

Capacitive tuning resolution

The capacitive tuning resolution is written as $V_{br} \times TE/2^B$, where V_{br} represents the gate oxide breakdown voltage, TE denotes the tuning slope efficiency (in pm/V), and B represents the number of bits in the

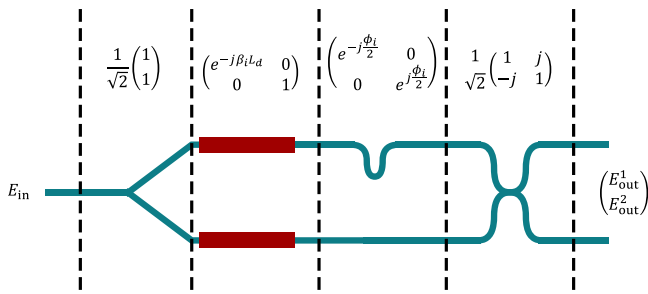


Fig. 8 | Transfer function of an imbalanced MZI. Schematic of an imbalanced MZI with lossless components including Y-junction, phase-shifter, delay line, and 50% directional coupler. The transfer matrix of each component is annotated.

counter. Considering the quality factor of the micro-rings (resulting in a slope efficiency of about 130 pm/V) and V_{br} of 5 V, a 5-bit counter is chosen, providing a resolution of approximately 2% in optical power, which is sufficient given the desired performance of the system.

MZI based Mux/DeMux monitoring

The tuning process of an MZI-based DeMux system is notably more complex compared to a DeMux employing drop ring resonators. In a ring-based setup, individual ring resonators are adjusted to maximize the output power. However, in an MZI-based system driven by a multi-frequency comb input, establishing the desired tuning point for each device cannot be solely deduced from their output power.

This section elaborates on the MZI tuning challenge through an analysis of the response of a lossless MZI to a multi-frequency source with the same per-mode power and a spacing of $\text{FSR}/2$, where FSR represents the free spectral range of the MZI set by the delay imbalance between the two arms.

For a lossless MZI shown in Fig. 8, with a Y-junction at the input, phase-shifters on both arms, a delay length of L_d on the top arm, and a 50% coupler at the output, the E-field transfer function can be expressed as

$$\begin{pmatrix} E_{\text{out}}^1 \\ E_{\text{out}}^2 \end{pmatrix} = \frac{1}{2} \begin{pmatrix} e^{-j(\beta_i L_d + \frac{\phi_i}{2})} + j e^{\frac{j\phi_i}{2}} \\ -j e^{-j(\beta_i L_d + \frac{\phi_i}{2})} + e^{\frac{j\phi_i}{2}} \end{pmatrix} E_{\text{in}}, \quad (1)$$

where E_{out}^1 and E_{out}^2 represent the electric fields at two outputs of the MZI. Here, $\pm \phi_i/2$ denotes the phase shift introduced by a phase shifter for an optical signal with frequency f_i . Note that the phase shifters on the top and bottom arms are driven differentially such that the overall phase shift of ϕ_i is achieved between the two arms. Also, L_d and β_i represent the delay imbalance between the two arms and the propagation constant of the optical signal with frequency f_i , respectively. Both β_i and ϕ_i are defined for a single tone signal with a frequency of f_i and can be expressed as

$$\beta_i = \frac{2\pi f_i}{\text{FSR}} \cdot \frac{1}{L_d}, \quad (2)$$

$$\frac{\phi_i}{2} = \frac{2\pi \Delta n L_{\text{ph}} f_i}{c}, \quad (3)$$

where Δn is the change in refractive index of the waveguide caused by one phase shifter, and L_{ph} and c represent the length of the phase shifter and the speed of light, respectively. For the case that the input optical signal consists of two single-tone waves at frequencies f_0 and $f_0 + \frac{\text{FSR}}{2}$, each with a similar power of P_0 , the input E-field can be

represented as

$$E_{\text{in}} = \sqrt{P_0} e^{j2\pi f_0 t} + \sqrt{P_0} e^{j2\pi(f_0 + \frac{\text{FSR}}{2})t}. \quad (4)$$

The total E-field at the top output is written as

$$E_{\text{out}}^1 = \frac{\sqrt{P_0}}{2} \left(e^{-j(\frac{2\pi f_0}{\text{FSR}} + \frac{\phi_1}{2})} + j e^{\frac{j\phi_1}{2}} \right) e^{j2\pi f_0 t} + \frac{\sqrt{P_0}}{2} \left(e^{-j(\frac{2\pi f_0}{\text{FSR}} + \pi + \frac{\phi_2}{2})} + j e^{\frac{j\phi_2}{2}} \right) e^{j2\pi(f_0 + \frac{\text{FSR}}{2})t}, \quad (5)$$

where ϕ_1 and ϕ_2 represent the phase shift caused by the phase shifters for the first and second tones, respectively. Using Eq. 5, we can derive the total photo-detected output power, which excluding the low frequency terms can be written as

$$P_{\text{out}}^1 = \frac{P_0}{2} \left(1 + \sin\left(\frac{2\pi f_0}{\text{FSR}} + \phi_1\right) - \sin\left(\frac{2\pi f_0}{\text{FSR}} + \phi_2\right) \right), \quad (6)$$

Which can be expressed as a function of the phase shift mismatch, $(\phi_2 - \phi_1)$, as

$$P_{\text{out}}^1 = P_0 \left(1 - \sin\left(\frac{\phi_2 - \phi_1}{2}\right) \sin\left(\frac{4\pi f_0}{\text{FSR}} + \phi_1 + \phi_2\right) \right), \quad (7)$$

If each phase shifter can induce a maximum phase shift of $|\phi_i| < \pi$, which is a reasonable assumption for practical cases, the maximum absolute change in the index of refraction can be determined using Eq. 3 as

$$\max_{\phi < \pi} |\Delta n| = \frac{c}{4f_0 L_{\text{ph}}}. \quad (8)$$

Using Eq. 8 and Eq. 3 the maximum phase shift mismatch can be approximated as

$$\max \left| \frac{\phi_2 - \phi_1}{2} \right| = \frac{2\pi L_{\text{ph}}}{c} \left(f_0 + \frac{\text{FSR}}{2} - f_0 \right) |\Delta n|_{\text{max}} = \frac{\pi}{2} \cdot \frac{\text{FSR}}{f_0}. \quad (9)$$

Given $\frac{\text{FSR}}{f_0}$ is in the order of 10^3 , the phase shift mismatch, $(\phi_2 - \phi_1)$, is small enough that the second term in Eq. 7 can be neglected, which indicates that the output power of the top arm remains unchanged regardless of the values of f_0 and Δn , that is

$$P_{\text{out}}^1 \cong P_0 \text{ for all values of } f_0 \text{ and } \Delta n. \quad (10)$$

Given the symmetry in the transfer matrix of the MZI, this analysis has a similar outcome for the second output of the MZI (P_{out}^2).

Reporting summary

Further information on research design is available in the Nature Portfolio Reporting Summary linked to this article.

Data availability

The data that support the findings of this study are available from the corresponding author upon request.

References

- Anashkina, E. A. et al. Microsphere-based optical frequency comb generator for 200 GHz spaced WDM data transmission system. In *Photonics*. Multidisciplinary Digital Publishing Institute (2020).
- Daudlin, S. et al. Integrated Kerr Comb Link with Multi-Channel DWDM Silicon Photonic Receiver. in *CLEO: Science and Innovations*. Optica Publishing Group (2022).

3. Li, C. et al. Hybrid WDM-MDM transmitter with an integrated Si modulator array and a micro-resonator comb source. *Opt. Express* **29**, 39847–39858 (2021).
4. Marin-Palomo, P. et al. Microresonator-based solitons for massively parallel coherent optical communications. *Nature* **546**, 274–279 (2017).
5. Moss, D. *Ultra-High Bandwidth Fiber-Optic Data Transmission With a Kerr Microcomb Chip Source* 6–11 (2021).
6. Pfeifle, J. et al. Coherent terabit communications with micro-resonator Kerr frequency combs. *Nat. photonics* **8**, 375–380 (2014).
7. Rizzo, A. et al. Massively scalable Kerr comb-driven silicon photonic link. *Nat. Photonics* **17**, 781–790 (2023).
8. Tan, M. et al. Optical data transmission at 44 terabits/s with a Kerr soliton crystal microcomb. in *Next-Generation Optical Communication: Components, Sub-Systems, and Systems X*. SPIE (2021).
9. Wang, F. X. et al. Quantum key distribution with on-chip dissipative Kerr soliton. *Laser Photonics Rev.* **14**, 1900190 (2020).
10. Wang, Y. et al. Scalable architecture for sub-pJ/b multi-Tbps comb-driven DWDM silicon photonic transceiver. in *Next-Generation Optical Communication: Components, Sub-Systems, and Systems XII*. SPIE (2023).
11. Chang, L., Liu, S. & Bowers, J. E. Integrated optical frequency comb technologies. *Nat. Photonics* **16**, 95–108 (2022).
12. Moss, D. Ultra-high bandwidth radio frequency and microwave photonic signal processing based on Kerr Micro-Combs. *SSRN Electron. J.* (2021).
13. Yu, S.-P. et al. A continuum of bright and dark-pulse states in a photonic-crystal resonator. *Nat. Commun.* **13**, 3134 (2022).
14. London, Y. et al. Energy efficiency analysis of comb source carrier-injection ring-based silicon photonic link. *IEEE J. Sel. Top. Quantum Electron.* **26**, 1–13 (2019).
15. Effenberger, F. J. & Zhang, D. WDM-PON for 5G wireless fronthaul. *IEEE Wirel. Commun.* **29**, 94–99 (2022).
16. El-Nahal, F. et al. A bidirectional wavelength division multiplexed (WDM) free space optical communication (FSO) system for deployment in data center networks (DCNs). *Sensors* **22**, 9703 (2022).
17. Kong, D. et al. Intra-datacenter interconnects with a serialized silicon optical frequency comb modulator. *J. Lightw. Technol.* **38**, 4677–4682 (2020).
18. Lima, E. S. et al. Integrated optical frequency comb for 5G NR Xhuals. *Sci. Rep.* **12**, 16421 (2022).
19. Notaro, P. et al. An optical transceiver reliability study based on sfp monitoring and os-level metric data. in *2023 IEEE/ACM 23rd International Symposium on Cluster, Cloud and Internet Computing (CCGrid)* IEEE. (2023).
20. Jin, W. et al. Hertz-linewidth semiconductor lasers using CMOS-ready ultra-high-Q microresonators. *Nat. Photonics* **15**, 346–353 (2021).
21. Siew, S. Y. et al. Review of silicon photonics technology and platform development. *J. Lightw. Technol.* 4374–4389 (2021).
22. Wang, L. et al. Athermal arrayed waveguide gratings in silicon-on-insulator by overlaying a polymer cladding on narrowed arrayed waveguides. *Appl. Opt.* **51**, 1251–1256 (2012).
23. Lu, Z. et al. Performance prediction for silicon photonics integrated circuits with layout-dependent correlated manufacturing variability. *Opt. express* **25**, 9712–9733 (2017).
24. Xing, Y. et al. Capturing the effects of spatial process variations in silicon photonic circuits. *ACS Photonics* **10**, 928–944 (2022).
25. Akiyama, T. et al. An extremely low-crosstalk WDM demultiplexer with an automatic error-correction capability enabling temperature insensitivity and high-yield integration on low-end Si PICs. in *45th European Conference on Optical Communication (ECOC 2019)*. IET (2019).
26. Geng, Z. et al. Photonic integrated circuit implementation of a sub-GHz-selectivity frequency comb filter for optical clock multiplication. *Opt. Express* **25**, 27635–27645 (2017).
27. Grillanda, S. et al. Wavelength locking of silicon photonics multiplexer for DML-based WDM transmitter. *J. Lightw. Technol.* **35**, 607–614 (2016).
28. Hu, T. et al. Thermally tunable filters based on third-order microring resonators for WDM applications. *IEEE Photonics Technol. Lett.* **24**, 524–526 (2012).
29. Padmaraju, K. et al. Wavelength locking of a WDM silicon microring demultiplexer using dithering signals. in *Optical Fiber Communication Conference*. Optica Publishing Group (2014).
30. Rizzo, A. et al. Ultra-broadband interleaver for extreme wavelength scaling in silicon photonic links. *IEEE Photonics Technol. Lett.* **33**, 55–58 (2020).
31. De, S. et al. CMOS-compatible photonic phase shifters with extremely low thermal crosstalk performance. *J. Lightw. Technol.* **39**, 2113–2122 (2021).
32. Ji, X. et al. Ultra-low-loss on-chip resonators with sub-milliwatt parametric oscillation threshold. *Optica* **4**, 619–624 (2017).
33. Lugiato, L. A. & Lefever, R. Spatial dissipative structures in passive optical systems. *Phys. Rev. Lett.* **58**, 2209 (1987).
34. Zang, J. et al. Laser power consumption of soliton formation in a bidirectional Kerr resonator. *Nat. Photon.* **19**, 510–517 (2025).
35. Yu, S.-P. et al. Spontaneous pulse formation in edgeless photonic crystal resonators. *Nat. Photonics* **15**, 461–467 (2021).
36. Zang, J. et al. *High-efficiency microcombs aligned with ITU-T grid for WDM optical interconnects*. in *Optical Fiber Communication Conference*. Optica Publishing Group (2023).
37. Zang, J. et al. Near unit efficiency in microresonator combs. in *CLEO: Science and Innovations* Optica Publishing Group (2022).
38. Jung, H. et al. Tantala Kerr nonlinear integrated photonics. *Optica* **8**, 811–817 (2021).
39. Absil, P. P. et al. Silicon photonics integrated circuits: a manufacturing platform for high density, low power optical I/O's. *Opt. Express* **23**, 9369–9378 (2015).
40. Chen, C.-H. et al. A comb laser-driven DWDM silicon photonic transmitter based on microring modulators. *Opt. Express* **23**, 21541–21548 (2015).
41. Cheung, S. et al. Ultra-power-efficient heterogeneous III–V/Si MOSCAP (de-) interleavers for DWDM optical links. *Photonics Res.* **10**, A22–A34 (2022).
42. Gevorgyan, H. et al. Miniature, highly sensitive MOSCAP ring modulators in co-optimized electronic-photonic CMOS. *Photonics Res.* **10**, A1–A7 (2022).
43. Pirmoradi, A. and F. Aflatouni. Monolithically integrated autonomous demultiplexers with near zero power consumption for beyond Tb/s Links. In *2023 Optical Fiber Communications Conference and Exhibition (OFC)*, IEEE (2023).
44. Omirzakhov K, Pirmoradi A, Hao H & Aflatouni F. Monolithic optical PAM-4 transmitter with autonomous carrier tracking. *Opt. Express* **32**, 2894–2905 (2024).
45. Zhang, Y. et al. A compact and low-loss Y-junction for submicron silicon waveguide. *Opt. Express* **21**, 1310–1316 (2013).
46. Akiyama, T. et al. Cascaded AMZ triplets: a class of demultiplexers having a monitor and control scheme enabling dense WDM on Si nano-waveguide PICs with ultralow crosstalk and high spectral efficiency. *Opt. Express* **29**, 7966–7985 (2021).
47. Rakowski, M. et al. 45nm CMOS-silicon photonics monolithic technology (45CLO) for next-generation, low power and high speed optical interconnects. In *Optical Fiber Communication Conference*. Optica Publishing Group (2020).
48. Soref, R. & Bennett, B. Electrooptical effects in silicon. *IEEE J. quantum Electron.* **23**, 123–129 (1987).

Acknowledgements

This work was supported by Defense Advanced Research Projects Agency PIPES program (HR0011-19-2-0016).

Author contributions

A.P., S.P., and F.A. conceived the project idea, A.P. designed, simulated, and did the chip and PCB layout for the demultiplexer systems. K.O. designed some electronics blocks for demultiplexer systems. J.Z. and Y.J. designed and characterized the microcomb. A.P. and Z.Y. conducted measurements of the full system. S.P. directed and supervised the comb design and characterization. F.A. directed and supervised the project. A.P., J.Z., S.P., and F.A. wrote the manuscript.

Competing interests

The authors declare no competing interests.

Additional information

Supplementary information The online version contains supplementary material available at <https://doi.org/10.1038/s41467-025-61288-x>.

Correspondence and requests for materials should be addressed to Firooz Aflatouni.

Peer review information *Nature Communications* thanks the anonymous reviewer(s) for their contribution to the peer review of this work. A peer review file is available.

Reprints and permissions information is available at <http://www.nature.com/reprints>

Publisher's note Springer Nature remains neutral with regard to jurisdictional claims in published maps and institutional affiliations.

Open Access This article is licensed under a Creative Commons Attribution-NonCommercial-NoDerivatives 4.0 International License, which permits any non-commercial use, sharing, distribution and reproduction in any medium or format, as long as you give appropriate credit to the original author(s) and the source, provide a link to the Creative Commons licence, and indicate if you modified the licensed material. You do not have permission under this licence to share adapted material derived from this article or parts of it. The images or other third party material in this article are included in the article's Creative Commons licence, unless indicated otherwise in a credit line to the material. If material is not included in the article's Creative Commons licence and your intended use is not permitted by statutory regulation or exceeds the permitted use, you will need to obtain permission directly from the copyright holder. To view a copy of this licence, visit <http://creativecommons.org/licenses/by-nc-nd/4.0/>.

© The Author(s) 2025